Theoretical calculations to identify and design transition metal-based additives for hydrogen storage materials

Thi Thu Le, Jiangming Cao, Svetlana Korneychuk, Wei-che Chang, Marcus Willi Rackel, Denis Kramer, Jürgen Markmann, Fahim Karimi, Astrid Pundt, Thomas Klassen, Claudio Pistidda

PII: S1385-8947(25)07768-X

DOI: https://doi.org/10.1016/j.cej.2025.166929

Reference: CEJ 166929

To appear in:

Received date: 23 May 2025

Revised date: 16 July 2025

Accepted date: 6 August 2025

Please cite this article as: T.T. Le, J. Cao, S. Korneychuk, et al., Theoretical calculations to identify and design transition metal-based additives for hydrogen storage materials, (2024), https://doi.org/10.1016/j.cej.2025.166929

Theoretical Calculations to Identify and Design Transition Metal-based Additives for Hydrogen Storage Materials

Thi Thu Le[a,*], Jiangming Cao[b], Svetlana Korneychuk[c,d,e], Wei-che Chang[a], Marcus Willi Rackel[f], Denis Kramer[b,*], Jürgen Markmann[a,g], Fahim Karimi[a], Astrid Pundt[c,d], Thomas Klassen[a,b] and Claudio Pistidda[a,*]

[a] Institute of Hydrogen Technology, Materials Design, Helmholtz-Zentrum hereon GmBH, Max-Planck Str. 1, 21502 Geesthacht, Germany

[b] Helmut Schmidt University, University of the Federal Armed Forces Hamburg, 22043 Hamburg, Germany

[c] Institute for Applied Materials – Materials Science and Engineering (IAM-WK), Karlsruhe Institute of Technology, Kaiserstraße 12, 76131 Karlsruhe, Germany

[d] Karlsruhe Nano Micro Facility (KNMFi), Karlsruhe Institute of Technology, Herrmann-von-Helmholtz-Platz 1, 76344 Eggenstein-Leopoldshafen, Germany

[e] Institute of Nanotechnology, Karlsruhe Institute of Technology, Hermann-von-Helmholtz-Platz 1, 76344 Eggenstein-Leopoldshafen, Germany

[f] Institute of Materials Physics, Helmholtz-Zentrum hereon GmbH, Max-Planck-Str. 1, D-21502 Geesthacht, Germany

[g] Institute of Materials Physics and Technology, Hamburg University of Technology, Eißendorfer Str. 42, 21073 Hamburg, Germany

*Corresponding authors: thi.le@hereon.de (T. T. Le); claudio.pistidda@hereon.de (C. Pistidda); d.kramer@hsu-hh.de (D. Kramer)

Abstract: This study demonstrates the successful design of transition metal boride-based additives to enhance the hydrogen absorption and desorption kinetics of hydrogen storage materials. Density functional theory (DFT) was used to predict a range of boride compounds, with (Ta:Ti)B_2 and (Nb:Ti)B_2 identified as promising candidates. In particular, the $Nb_{1/2}Ti_{1/2}B_2$ and $Ta_{1/2}Ti_{1/2}B_2$ compositions significantly improve the kinetic properties of the 2LiH-MgB_2 (LiMgB) system. When small amount of these additives is incorporated into LiMgB, its kinetics is improved twice in comparison to the undoped material while maintaining stable reversibility. This substantial improvement is attributed to the presence of $Nb_{1/2}Ti_{1/2}B_2$ and $Ta_{1/2}Ti_{1/2}B_2$ nanoparticles, which act as heterogeneous nucleation sites for MgB_2. The study highlights how computational methods can accelerate the design and discovery of optimal additive compositions for hydrogen storage, minimizing the need for extensive experimental testing.

Keywords: hydrogen storage, DFT, transition metal borides, additive, material design

1. Introduction

Hydrogen is widely recognized as a promising energy carrier for sustainable energy systems due to its high gravimetric energy density and environmental friendliness [1, 2]. However, its intrinsically low volumetric energy density at ambient conditions (e.g. 4.8 MJ/L at 700 bar) [3] is a significant barrier, highlighting the critical need for efficient and practical storage solutions.

Conventional hydrogen storage methods, such as liquefaction and compression, are both costly and have safety concerns. Adsorption on high surface area materials such as zeolites, carbon-based compounds and MOFs is a promising alternative, although effective uptake typically requires cryogenic temperatures [4] and current materials do not meet DOE targets at ambient conditions [5]. Hydrogen clathrate hydrates offer molecular storage but require extreme pressures (~ 3000 bar at 77 °C) or additives such as THF [6, 7]. In contrast, atomic storage in metal hydrides offers higher volumetric densities and safer operation at moderate conditions [8]. Common metal hydrides (e.g. TiFe, $Ti_{1.1}CrMn$) suffer from low gravimetric capacities [9, 10], while complex hydrides such as $LiBH_4$ offer superior gravimetric (18.5 wt.%) and volumetric (121 kg H_2/m^3) capacities [11, 12], but are hampered by high thermodynamic stability and poor reversibility. To overcome these limitations, reactive hydride composites (RHCs) - formed by combining complex and simple hydrides (e.g. $2LiBH_4$-MgH_2, $2NaBH_4$-MgH_2, $Mg(NH_2)_2$-$2LiH$) have been proposed to improve kinetics and thermodynamics [13]. In such composite hydrides, an exothermic reaction between the hydride components during dehydrogenation stabilizes the products, reducing the overall reaction enthalpy and allowing full reversibility while maintaining high hydrogen capacity [14-17]. However, their complex reaction pathways result in sluggish kinetics. Mechanical processes such as ball milling [18], cold rolling [19] and high pressure torsion [20] can improve hydrogen storage properties, although the effects are often short-lived due to particle growth and agglomeration during cycling. To achieve long-term improvements, nanostructured transition metal (TM)-based additives have proven effective in both complex hydrides and RHCs [21-25]. In systems such as $2LiBH_4$-MgH_2/$2LiH$-MgB_2 (referred to as LiMgB), nano-sized additives like transition metal borides MB_2 (M = Ti, Al, V, Zr, Sc) [22, 23] or $AlTi_3$ [21] enhance dehydrogenation by providing energetically favourable sites for MgB_2 nucleation. This improvement is attributed to the structural compatibility between MB_2 (or $AlTi_3$) and MgB_2, including crystallographic similarity with small interplanar mismatch (< 6 %) and interatomic spacing misfit (< 10%) along certain directions [26, 27]. All the catalysts studied exhibit crystallographic matching with MgB_2, which minimizes the interfacial strain energy and therefore facilitates the formation of the MgB_2 phase during dehydrogenation.

Several investigations have focused on tailoring the lattice constants to improve the catalytic activity of nucleation processes. Nucleation catalysts with lattice spacings close to those of the nucleating crystal can reduce the nucleation barrier and improve catalytic efficiency by promoting epitaxial growth and interfacial pre-ordering [28-30]. For example, modification of lattice parameters by alloying elements can optimize interfacial strain and electronic properties, thereby enhancing catalytic performance [29]. In addition, surface lattice engineering has been used to fine-tune the lattice mismatch between seed nanocrystals and deposited materials, allowing precise control over spatial configurations and improving catalytic behaviour in hybrid nanocrystals [31]. Taken together, these approaches use lattice matching and strain engineering to tailor active sites, thereby improving nucleation and catalytic processes [32].

Based on these observations, and with the aim of finding novel additives to improve the kinetic properties of the LiMgB system, we propose tuning the lattice constant of TiB_2 by partially substituting Ti with other transition metals, such as Nb or Ta, to achieve a closer match with the lattice of MgB_2. The low interfacial energy between TiB_2 and MgB_2 facilitates the heterogeneous nucleation of MgB_2 on TiB_2 surfaces, making TiB_2 an effective nucleation substrate [33]. Furthermore, studies indicate that NbB_2 and TaB_2 exhibit good lattice compatibility with TiB_2, facilitating interfacial coherence between these phases. In contrast, ScB_2, YB_2, ZrB_2, and HfB_2 demonstrate significant lattice mismatch with TiB_2, which restricts their ability to form coherent interfaces and thus limits their mutual interfacial compatibility [34]. The lattice similarities are expected to promote the formation of more coherent interfaces and facilitate MgB_2 nucleation during dehydrogenation. In this study, we combine DFT calculations and experimental approaches to identify effective additives, i.e. $(Nb:Ti)B_2$ and $(Ta:Ti)B_2$, that can effectively enhance the kinetic properties of the LiMgB composite system. Two representative compositions $Nb_{1/2}Ti_{1/2}B_2$ and $Ta_{1/2}Ti_{1/2}B_2$ are investigated in detail. The results are presented in the following sections.

2. Experimental Method

2.1. Materials preparation

All raw materials were purchased from commercial suppliers without further modification: lithium hydride (LiH, 95% purity, Sigma-Aldrich), magnesium boride (MgB_2, 99% purity, Alfa Aesar), and metal species (Ti, Nb, Ta and B, > 99% purity, Sigma-Aldrich). $Nb_{1/2}Ti_{1/2}B_2$ and $Ta_{1/2}Ti_{1/2}B_2$ compositions were prepared by arc melting a mixture of Nb/or Ta, Ti and B in a molar ratio of 0.5:0.5:2. The ingots, after being arc-melted, were crushed into small particles. The morphologies of $Nb_{1/2}Ti_{1/2}B_2$ and $Ta_{1/2}Ti_{1/2}B_2$ are discussed in the subsequent sections. For the synthesis of the LiMgB, MgB_2 was mixed with LiH in a molar ratio of 1:2. This mixture was ball milled in a stainless-steel vial for 300 min with a ball-to-powder ratio (BPR) of 20:1. To dope the mixture with X additives (X = $Nb_{1/2}Ti_{1/2}B_2$ or $Ta_{1/2}Ti_{1/2}B_2$), 5 wt.% and 10 wt.% of X (with selected particle size of less than 90 μm) were added to the LiMgB mixture. These doped samples were then ball milled for 300 min with a ball-to-powder ratio (BPR) of 20:1. The preparation of the materials was carried out in MBraun gloveboxes that had a controlled oxygen and humidity atmosphere (< 1 ppm of O_2 and H_2O) to keep the samples from oxidizing.

2.2. Materials characterization

Ex situ powder X-ray diffraction (XRD) measurements were performed using a D8 Discover diffractometer (Bruker AXS GmbH, Karlsruhe, Germany) equipped with a Cu Kα radiation (wavelength λ = 1.54184 Å) and a 2D VANTEC detector. Diffractograms were recorded over a 2θ range of 10° to 90°, in nine steps and an exposure time of 300 s per step. To prevent oxidation, a small amount of sample was placed in a flat commercial sample holder inside an argon-filled glovebox (oxygen and moisture concentration $\leq$ 1 ppm) and sealed with an airtight lid made of poly(methylmethacrylate).

Hydrogenation/dehydrogenation measurements, as well as kinetic behavior of the materials, were carried out using a home-built volumetric Sieverts-type apparatus. Initial dehydrogenation of certain samples was conducted from room temperature (RT) to 400 °C with a heating ramp of 3 °C/min under 3 bar of hydrogen (H_2) pressure. Hydrogenation/dehydrogenation cycling measurements for all materials were performed at 400 °C under 3 bar H_2 for dehydrogenation and at 350 °C under 50 bar H_2 for hydrogenation. The chosen temperature and pressure conditions are based on the published thermodynamic data and previous studies on the LiMgB composite system [13, 15].

The microstructure and elemental mapping of materials were characterized by scanning electron microscopy (SEM) (FEI Helios G4 PFIB) equipped with energy dispersive X-ray spectroscopy detector (EDAX Octane Elite Super). By scanning the electron beam across a predetermined area, the overall chemical composition was analyzed under 15kV. At least 5 areas were measured for each specimen to obtain the statistical results. The element mapping was measured in an area of 1500 μm × 1500 μm to investigate the element distribution.

To estimate the particle size distribution of the investigated samples, small-angle X-ray scattering (SAXS) experiments were carried out in a Xenocs Xeuss 3.0 system equipped with a Dectris Pilatus3 R 300K detector. A microfocus tube with a copper (Cu) anode operating at 50 kV and 0.6 mA served as X-ray source. To avoid any oxidation of the materials, all SAXS samples were prepared inside a glovebox with a continuously filled Argon flow. The powdered samples were placed inside a circular hole in an aluminum holder and sealed with Kapton tape. The SAXS signal of an empty cell, i.e. the signal of two Kapton tapes and the primary beam were measured separately with the same parameters and the one of the empty cells was subtracted from the measured patterns. For all SAXS measurements, the area of illumination on the samples was set to roughly 500x500 μm^2. The measurements were carried out at two sample-to-detector distances (SDD) at 800 mm and 1800 mm to cover the desired q-range, with an exposure time of 10800 s and 21600 s, respectively. The quantity q describes the magnitude of the scattering vector of the incident beam, which is given by: $q = (4\pi/\lambda)\, sin\, \theta$, where 2θ is the scattering angle of the elastically scattered photons and λ is the corresponding monochromatic wavelength. All the fits of the reduced scattering data were done by SASfit software [35] assuming a polydisperse spherical particle model as a first approximation.

Scanning transmission electron microscopy (STEM) measurements were carried out on a probe aberration-corrected Thermo Fisher Scientific Themis Z microscope at 300 kV. EDS maps were acquired using a Super-X EDX detector. The sample was drop-casted from the toluene solution on the lacey-carbon TEM grid in the glovebox with the Ar gas environment. The sample was delivered to the microscope in the Gatan vacuum transfer holder.

2.3. Computational Method

The total energy calculations are carried out with the Vienna Ab initio Simulation package (VASP) [36-38] within framework of density functional theory (DFT), performed the Perdew-Burke-Ernzerhof (PBE) [39] functional with projected waves (PAW) [40]. The cutoff energy is set to 520 eV, The energy convergence threshold for electronic steps is 10^{-3} eV, whereas the convergence tolerance of maximal atomic force is less than 10^{-2} eV/Å. The enumerated configurations are generated by CASM [41-45], using the cluster expansion model. Considering each configuration σ_i is weighted based on its distance from the convex hull (Eq. 1):

$$\omega(\sigma_i) = \exp \frac{E(\sigma_i) - E_{\mathrm{hull}}(x_i)}{k_{\mathrm{B}}\tilde{T}} \qquad \text{(Eq. 1)}$$

where $E(\sigma_i)$ denotes the formation energy for each configuration σ_i. k_B is Boltzmann constant, and $\tilde{T}$ is temperature. $E_{\mathrm{hull}}(x_i)$ represents the formation energy of the convex hull under corresponding concentration (x).

3. Results and Discussion

3.1. Designing transition metal borides-based additives based on DFT calculations

In the development of transition metal boride-based additives for improving the hydrogen storage performance of the LiMgB, the introduction of boron is often unavoidable, leading to the formation of ternary alloys. It is essential to investigate which alloys are easier to form and how specific borides affect the properties of hydrogen storage materials. One key approach is to modify the lattice constant of TiB_2 by alloying TiB_2 with other elements to closely match that of MgB_2. TiB_2 crystallizes in a hexagonal *P6/mmm* structure (space group, *s.g.* no. 191) with calculated equilibrium lattice parameters of $a = b = 3.035$ Å and $c = 3.223$ Å, forming a hexagonal prism coordination. By adjusting the lattice constants, nucleation of the MgB_2 phase could be made more difficult or kinetically less favorable. Several elements close to titanium in the periodic table, particularly those with crystal structures similar to TiB_2, were considered as potential candidates for alloying. The primary aim is to alloy or combine TiB_2 with elements such as Sc, Y, Zr, Hf, Nb and Ta. Several boride-like structures with larger lattice constants than TiB_2 were identified (as shown in **Table S1**). The formation energy of the $(M{:}Ti)B_2$ alloys (M = Mg, Sc, Y, Zr, Hf, Nb and Ta) over different compositions, as shown in **ESI-Figures S1-S3**, suggests that only $(Nb{:}Ti)B_2$ and $(Ta{:}Ti)B_2$ break the convex hull, while $(Zr{:}Ti)B_2$ and $(Y{:}Ti)B_2$ show phase separation, and $(Sc{:}Ti)B_2$ and $(Hf{:}Ti)B_2$ slightly deviate the convex hull.

As shown in **Figure 1a**, the predicted $(Nb{:}Ti)B_2$ alloy shows a novel ternary ground state that breaks the convex hull and has low zero-temperature formation energy over the entire range of concentrations considered. From the Nb-rich (left) to the Ti-rich side (right), nine ternary borides breaking the convex-hull (connected by red solid lines) have an advantage over other corresponding concentrations. These include $Nb_{7/8}Ti_{1/8}B_2$, $Nb_{1/2}Ti_{1/2}B_2$, $Nb_{4/9}Ti_{5/9}B_2$, $Nb_{1/3}Ti_{2/3}B_2$, $Nb_{2/9}Ti_{7/9}B_2$, $Nb_{1/6}Ti_{5/6}B_2$, and $Nb_{1/9}Ti_{8/9}B_2$. Similarly, as shown in **Figure 1b**, the predicted compositions for (Ta:Ti)B_2 include $Ta_{7/8}Ti_{1/8}B_2$, $Ta_{7/9}Ti_{2/9}B_2$, $Ta_{5/9}Ti_{4/9}B_2$, $Ta_{1/2}Ti_{1/2}B_2$, $Ta_{4/9}Ti_{5/9}B_2$, $Ta_{1/3}Ti_{2/3}B_2$, $Ta_{2/9}Ti_{7/9}B_2$, $Ta_{1/6}Ti_{5/6}B_2$, and $Ta_{1/9}Ti_{8/9}B_2$. These calculations show that the (Nb:Ti)B_2 and (Ta:Ti)B_2 alloys are predicted to form solid solutions, with changes in lattice constant following Vegard's law.

While $Nb_{1/3}Ti_{2/3}B_2$ and $Ta_{1/3}Ti_{2/3}B_2$ show the lowest formation energies, the negative formation energies of $Nb_{1/2}Ti_{1/2}B_2$ and $Ta_{1/2}Ti_{1/2}B_2$ likewise suggest that these compounds are thermodynamically favorable and likely to form under suitable synthesis conditions. Notably, the calculated surface energies of $Nb_{1/2}Ti_{1/2}B_2$ and $Ta_{1/2}Ti_{1/2}B_2$ interfaced with TiB_2 are 3.84 and 3.89 J/m^2, respectively, which are lower than those of $Nb_{1/3}Ti_{2/3}B_2$ and $Nb_{1/3}Ti_{2/3}B_2$ (see **ESI-Table S2**). Projected density of state (DOS) analysis shows that the Ti d-orbitals dominate the electronic states near the Fermi-level in $M_{1/2}Ti_{1/2}B_2$ (M = Nb, Ta), as illustrated in **ESI-Figure S4b** and **ESI-Figure S5b.** As expected, increasing the Ti concentration results in greater Ti d-state contributions near the Fermi level in $M_{1/3}Ti_{2/3}B_2$, as shown in **ESI-Figure S4c** and **ESI-Figure S5c**. In addition, the calculated DOS reveals a gradual shift in the d-band center (ε_d) within the ε_d range defined by MB_2 and TiB_2, as shown in **ESI-Figure S4 and S5**. Tunning the ε_d value via alloying or surface engineering can optimize the adsorption-desorption equilibrium, thereby enhancing catalytic performance for hydrogen storage [46-48]. Furthermore, as shown in **Figure 2**, the lattice parameters of $Nb_{1/2}Ti_{1/2}B_2$ and $Ta_{1/2}Ti_{1/2}B_2$ closely match those of MgB_2, further supporting for their structural compatibility. Taking structural, electronic, and thermodynamic factors into account, $Nb_{1/2}Ti_{1/2}B_2$ and $Ta_{1/2}Ti_{1/2}B_2$ were selected as representative compositions for further investigation of their effects on the hydrogen storage performance of the LiMgB system.

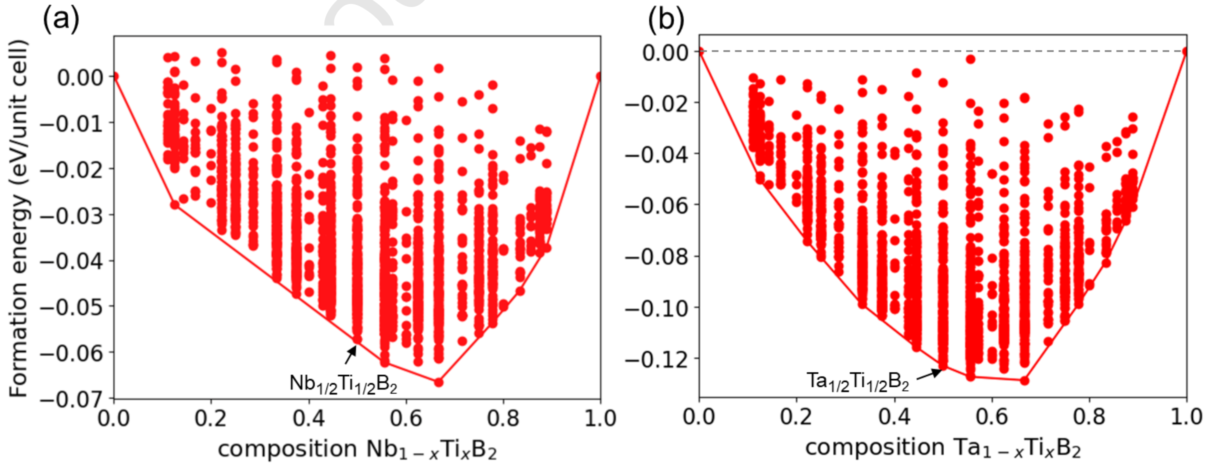

Figure 1. Formation energies in eV/unit cell predicted from DFT calculation across the tie-line composition of (**a**) $Nb_{1-x}Ti_xB_2$ and (**b**) $Ta_{1-x}Ti_xB_2$ alloys. Red lines mark the convex hull outline, representing the thermodynamic stability under the corresponding composition. The grey dashed line denotes the interhost convex hull.

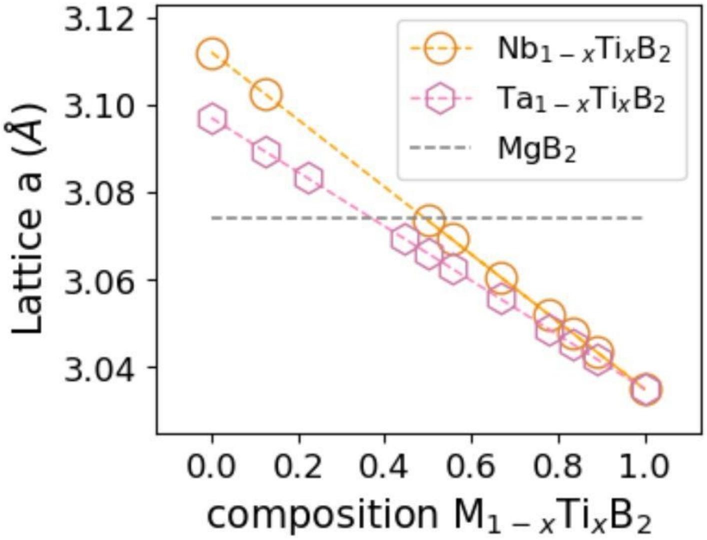

Figure 2. Lattice parameter *a* (Å) for $Ti_{1-x}Ti_xB_2$ and $Ta_{1-x}Ti_xB_2$, compared with MgB_2 according to Table S1.

Figure 3 shows XRD patterns and SEM-EDS images of the synthesized $Nb_{1/2}Ti_{1/2}B_2$ alloy. The XRD diffractogram (**Figure 3a**) shows Bragg peaks corresponding to a single hexagonal phase, consistent with the standard $Nb_{1/2}Ti_{1/2}B_2$ peaks of the *s.g. P6/mmm* (ICSD44458). The lattice parameters of the $Nb_{1/2}Ti_{1/2}B_2$ derived from the Rietveld refinement using MAUD software [49] of the XRD data (**ESI-Figure S6**) are $a = b = 3.0600$ Å, $c = 3.2560$ Å. In addition, there are small peaks (UP1) that could not be assigned to any known phase. The morphology of this additive ($Nb_{1/2}Ti_{1/2}B_2$) is analyzed in **Figure 3b-c**. The well-distributed presence of Nb, Ti and B elements at the same locations are observed, supporting the formation of a (Ta:Ti:B)-containing single phase (**Figure 3c**).

Similarly, the XRD and SEM-EDX data of the synthesized $Ta_{1/2}Ti_{1/2}B_2$ alloy is analyzed as shown in **Figure 4.** The XRD diffractogram (**Figure 4a**) indicates the presence of a single hexagonal phase (indexed as $Ta_{1/2}Ti_{1/2}B_2$) within the *s.g. P6/mmm* (ICSD44590). The lattice parameters of synthesized $Ta_{1/2}Ti_{1/2}B_2$ alloy deriving from XRD's Rietveld refinement (**ESI-Figure S7**) are $a = b = 3.055$ Å, $c = 3.2544$ Å. In addition, there are tiny peaks corresponding to the unknown phase (UP2). The EDS elemental mapping also reveals the distribution of Ta, Ti, and B elements, which appear to be located in largely similar regions (**Figure 4b-c**). However, the distribution of Ti and Ta on the EDX map is not entirely homogeneous. This could be attributed to the fact that the $Ta_{1/2}Ti_{1/2}B_2$ additive was synthesized by arc melting - a process involving extremely high plasma temperatures, leading to rapid solidification and potential volatilization of raw materials. To achieve the target stoichiometry, raw materials were incrementally added until the composition was confirmed by XRD analysis. Despite this careful procedure, minor compositional inhomogeneities remain. Nevertheless, the target phase corresponds to $Ta_{1/2}Ti_{1/2}B_2$ is successfully obtained, as confirmed by XRD (**Figure 4a**). The synthesized $Nb_{1/2}Ti_{1/2}B_2$ and $Ta_{1/2}Ti_{1/2}B_2$ phases closely match the corresponding standard patterns retrieved from the ICSD database.

According to the XRD and SEM-EDS analysis, the two compositions, $Nb_{1/2}Ti_{1/2}B_2$ and $Ta_{1/2}Ti_{1/2}B_2$, were successfully synthesized by arc melting with micro-sized particles, with lattice parameters between those of TiB_2 ($a = b$= 3.035 Å, c = 3.223 Å) and MgB_2 ($a = b$ = 3.074 Å, c = 3.534 Å). These two additives ($Nb_{1/2}Ti_{1/2}B_2$ and $Ta_{1/2}Ti_{1/2}B_2$), with selected particle size of less than 90 μm, were then incorporated into the LiMgB system, and their effects on its hydrogen storage properties were studied.

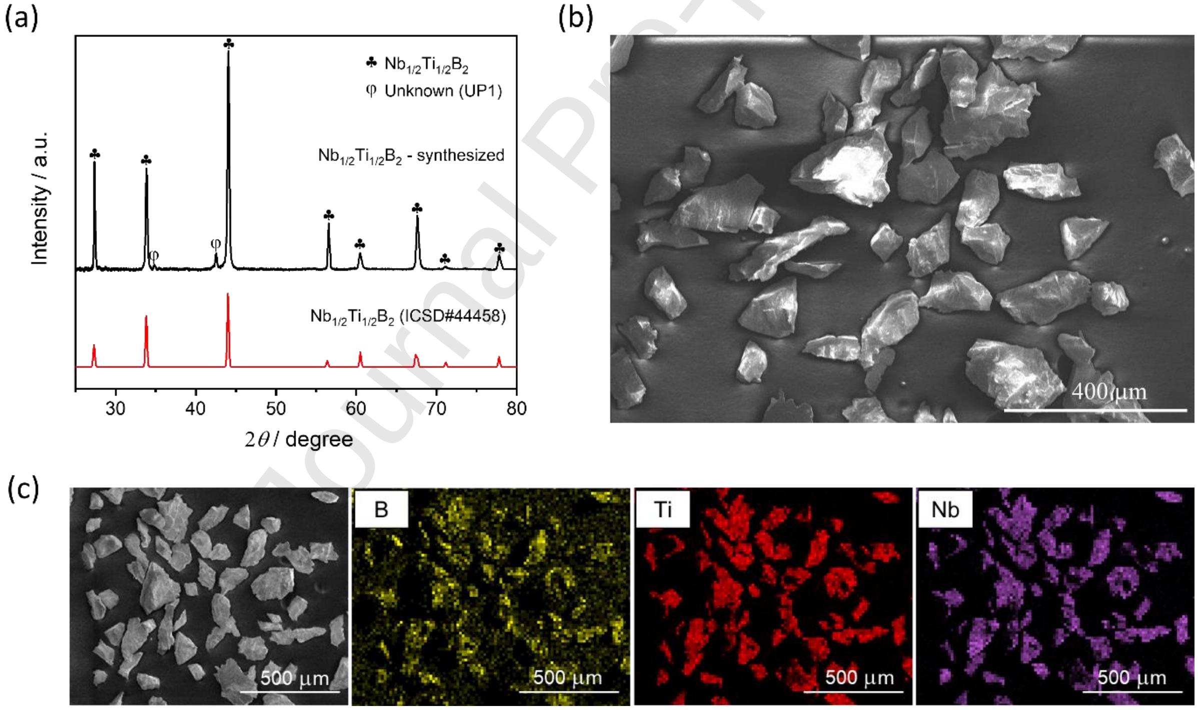

Figure 3. (**a**) XRD pattern, (**b**) SEM image of the synthesized $Nb_{1/2}Ti_{1/2}B_2$ alloy, and (**c**) EDS elemental mapping of Nb, Ti and B elements.

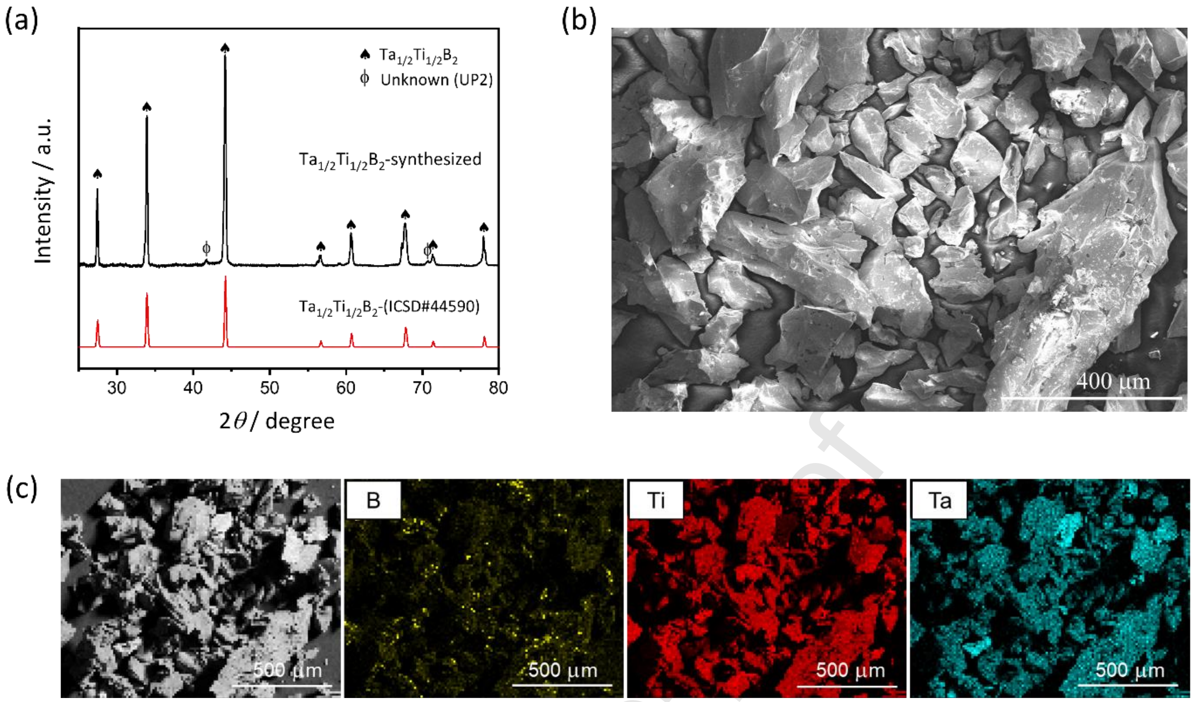

Figure 4. (**a**) XRD pattern, (**b**) SEM image of the synthesized Ta$_{1/2}$Ti$_{1/2}$B$_2$ alloy, and (**c**) EDS elemental mapping of Ta, Ti and B elements.

3.2. Effect of the Nb$_{1/2}$Ti$_{1/2}$B$_2$ and Ta$_{1/2}$Ti$_{1/2}$B$_2$ additives on the hydrogen storage properties of LiMgB system

XRD patterns of the pure and doped samples are shown in **Figure 5**. In **Figure 5a**, the diffractograms of pure materials (Nb$_{1/2}$Ti$_{1/2}$B$_2$ and LiMgB) are also observed in the LiMgB doped with Nb$_{1/2}$Ti$_{1/2}$B$_2$. For example, in the LiMgB-5wt.%Nb$_{1/2}$Ti$_{1/2}$B$_2$ composite sample, the Nb$_{1/2}$Ti$_{1/2}$B$_2$ peaks are detected in addition to the MgB$_2$ and LiH peaks, indicating no reaction between the host material (LiMgB) and the additive (Nb$_{1/2}$Ti$_{1/2}$B$_2$). Similarly, as shown in **Figure 5b**, the presence of Ta$_{1/2}$Ti$_{1/2}$B$_2$ peaks in the LiMgB-5wt.%Ta$_{1/2}$Ti$_{1/2}$B$_2$ sample along with LiH and MgB$_2$ peaks indicates that no reaction has occurred between LiMgB and Ta$_{1/2}$Ti$_{1/2}$B$_2$.

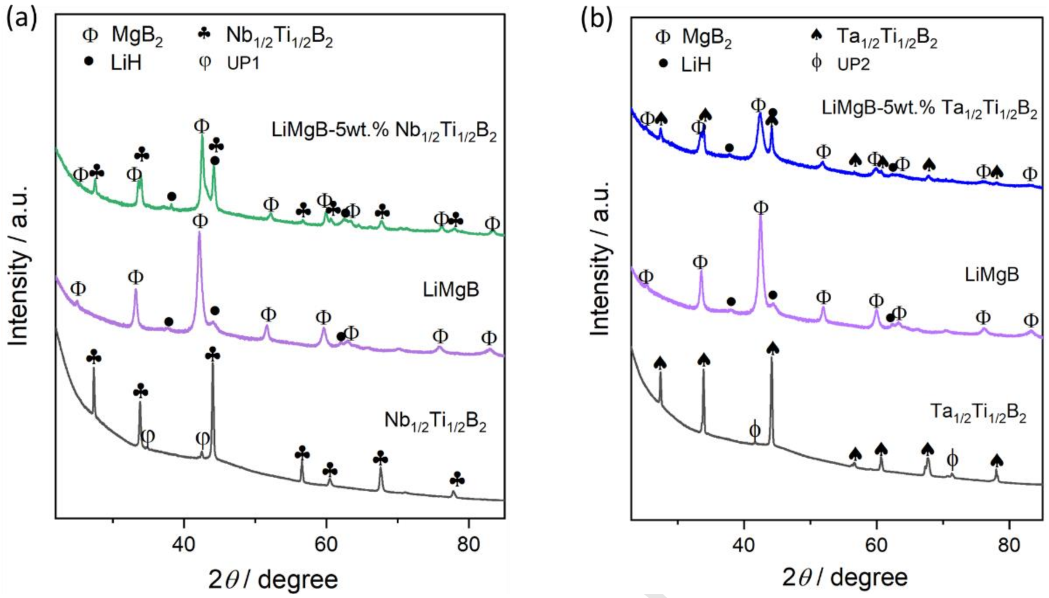

Figure 5. XRD data of (**a**) LiMgB-5wt.%$Nb_{1/2}Ti_{1/2}B_2$ and (**b**) LiMgB-5wt.%$Ta_{1/2}Ti_{1/2}B_2$ systems.

Figure 6 presents the first hydrogenation and dehydrogenation curves of the pure LiMgB compared to those of the doped LiMgB samples. In the first hydrogenation process, all the doped samples show fast kinetics exceeding those of pure LiMgB. The best hydrogenation performance is observed for the LiMgB doped with 10 wt.% $Nb_{1/2}Ti_{1/2}B_2$ (**Figure 6c**). After the first 4 hours of hydrogenation, the LiMgB-10wt.%$Nb_{1/2}Ti_{1/2}B_2$ has absorbed 8.6 wt.% H, compared to approximately 6 wt.% H; 6.2 wt.% H, and 5.3 wt.% H for the samples doped with 5 wt.% $Nb_{1/2}Ti_{1/2}B_2$, 5wt.% $Ta_{1/2}Ti_{1/2}B_2$, and 10 wt.% $Ta_{1/2}Ti_{1/2}B_2$, respectively. These values are higher than that of the pure LiMgB sample (~ 4.6 wt.% H) at the same conditions (see **inset graph**). Given the hydrogenation time, the maximum achievable hydrogen capacity of the pure LiMgB sample is slightly lower than that of the LiMgB samples doped with the $Nb_{1/2}Ti_{1/2}B_2$ additive, but higher than that of the samples doped with the $Ta_{1/2}Ti_{1/2}B_2$ additive. Nevertheless, the final hydrogen capacity achieved in all samples studied is lower than the theoretical hydrogen storage capacity of the LiMgB system (~ 11.45 wt.% H) [13], concerning the weight of additives added, the nonhomogeneous dispersion of additive species, and the not 100% purity of raw materials.

Similarly, the dehydrogenation kinetics for the doped LiMgB samples is also faster than that of the pure sample, with the best dehydrogenation kinetics observed in the sample doped with 10 wt.% $Nb_{1/2}Ti_{1/2}B_2$ (**Figure 6h**), In fact, the dehydrogenation of the LiMgB-based systems takes place in two consecutive steps [21]: the first step involving the decomposition of MgH_2 into Mg and H_2 (referred to Zone I) and the second step corresponding the reaction between Mg and $LiBH_4$ to form MgB_2, LiH and H_2 (referred to Zone II). The period between zone (I) and zone (II) is referred to as the incubation period for MgB_2 formation. However, in the samples studied, this incubation period was absent. The dehydrogenation kinetics of the LiMgB-

10wt.%$Nb_{1/2}Ti_{1/2}B_2$ sample was the fastest among the samples investigated, indicating relative fast nucleation and growth of MgB_2 during the second step of dehydrogenation reaction. The results observed from this investigation show that the addition of both $Nb_{1/2}Ti_{1/2}B_2$ and $Ta_{1/2}Ti_{1/2}B_2$ additives promotes the formation of MgB_2, resulting in enhanced hydrogenation/dehydrogenation kinetics of LiMgB composite system.

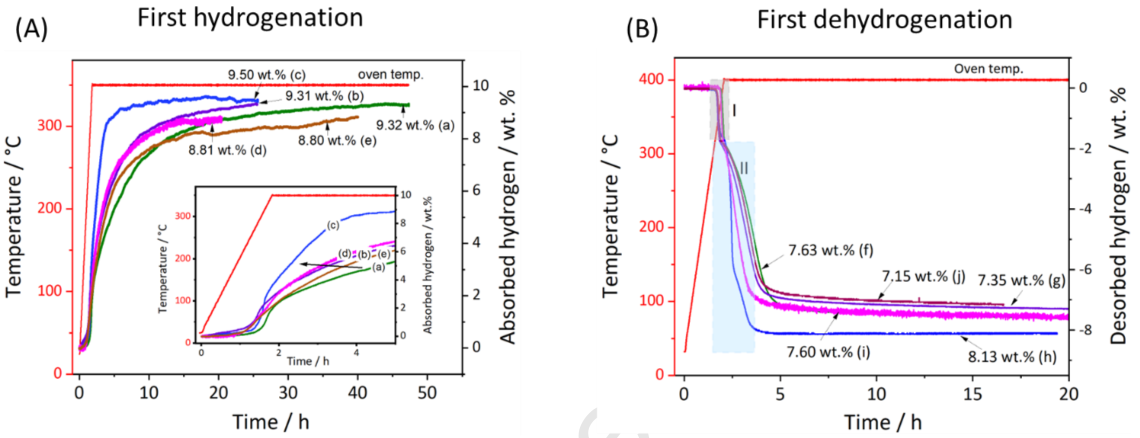

Figure 6. (**A**) The first hydrogenation kinetic data: (**a**) pure LiMgB and doped LiMgB samples: (**b**) LiMgB-5wt.%$Nb_{1/2}Ti_{1/2}B_2$; (**c**) LiMgB-10wt.%$Nb_{1/2}Ti_{1/2}B_2$; (**d**) LiMgB-5wt.%$Ta_{1/2}Ti_{1/2}B_2$, and (**e**) LiMgB-10wt.%$Ta_{1/2}Ti_{1/2}B_2$. Inset graph showing the hydrogenation data for all samples over the first 5h. (B) The first and dehydrogenation kinetic data: (**f**) pure LiMgB, (**g**) LiMgB-5wt.%$Nb_{1/2}Ti_{1/2}B_2$, (**h**) LiMgB-10wt.%$Nb_{1/2}Ti_{1/2}B_2$, (**i**) LiMgB-5wt.%$Ta_{1/2}Ti_{1/2}B_2$ and (**j**) LiMgB-10wt.%$Ta_{1/2}Ti_{1/2}B_2$.

The reversibility of the pure LiMgB and doped LiMgB samples over the subsequent five hydrogenation/dehydrogenation cycles is displayed in **Figure 7**. **Figures 7a-c** show the hydrogenation cycles, while **Figures 7d-f** depict the dehydrogenation of the pure and doped samples. In hydrogenation cycle tests, the doped samples (**Figures 7b, c**) demonstrate stable hydrogen absorption during cycling, although their overall hydrogen capacity is lower than the pure one (**Figure 7a**), probably due to the addition of additives. In particular, 95% of hydrogen is absorbed within 2 hours for doped samples, with progressively faster kinetics in subsequent cycles, compared to the pure LiMgB sample which requires 6 hours to achieve a comparable level of hydrogen absorption. Similarly, the dehydrogenation cycling performance is even more stable than that of hydrogenation, with a smaller drop in reversible hydrogen capacity for all samples. Especially, both doped samples (**Figure 7e, f**) complete hydrogen desorption in 3 hours compared to the pure LiMgB (approximately 6 hours, **Figure 7d**). During dehydrogenation, all samples show good reversibility, with a similar amount of absorbed hydrogen being desorbed accordingly, and the doped samples exhibiting the least decrease in reversible hydrogen capacity (**Figure 7g, h**). Besides, in region II, the curves for the LiMgB-10wt.%$Ta_{1/2}Ti_{1/2}B_2$ sample show the greatest stability of the samples investigated.

As also observed in **Figure 6**, the first hydrogenation and dehydrogenation of the LiMgB-10wt.%$Ta_{1/2}Ti_{1/2}B_2$ sample are slower compared to the LiMgB-5wt.%$Ta_{1/2}Ti_{1/2}B_2$ sample. But this comparison refers to the first hydrogen sorption cycle. In the subsequent cycles, the LiMgB sample with 10 wt.% $Ta_{1/2}Ti_{1/2}B_2$ (**Figure 7c, e**) shows a superior performance in the hydrogen cycle compared to the sample with 5 wt.% $Ta_{1/2}Ti_{1/2}B_2$ (**Figure S8**). This can be attributed to the initial advantage of the 5 wt.% $Ta_{1/2}Ti_{1/2}B_2$ sample, which shows a better hydrogen absorption/desorption behavior, probably due to a more uniform dispersion of the additive in the host matrix. However, with continued cycling at elevated temperatures, sintering of the particles reduces the catalytic activity. In this context, the LiMgB-10 wt.% $Ta_{1/2}Ti_{1/2}B_2$ sample, which has a higher catalytic reserve, maintains its activity more effectively, resulting in improved long-term performance. It should be noted that optimizing the exact number of additives to achieve the best hydrogen storage performance is beyond the scope of this study.

The results of these volumetric cycling tests indicate the beneficial effect of $Nb_{1/2}Ti_{1/2}B_2$ and $Ta_{1/2}Ti_{1/2}B_2$ on the hydrogen absorption/desorption properties of the LiMgB system. These two additives do not react with the host material (LiMgB) during the hydrogenation-dehydrogenation processes as their Bragg peaks are observed in the XRD data of the doped samples (**ESI-Figures S9-S10**). This suggests that these catalysts are highly stable and resistant to degradation processes or decomposition under the tested conditions. According to the SAXS analysis (**ESI-Figure S11**), the volume-weighted size distribution of the particles in the pure and doped LiMgB samples is similar, with a mean size of around 200 nm (see **Figure 8a**). However, it is important to note that it is not possible to separate the scattering contribution of specific elements from the SAXS data, meaning that the size distribution of the $Nb_{1/2}Ti_{1/2}B_2$ and $Ta_{1/2}Ti_{1/2}B_2$ particles are indistinguishable from other structures present in the sample. Despite this limitation, an example from the STEM-EDS investigation for the LiMgB-10 wt.% $Ta_{1/2}Ti_{1/2}B_2$ sample shows that the particle sizes for $Ta_{1/2}Ti_{1/2}B_2$ range from appx. 150 nm to 230 nm (see **Figure 8b**), confirming the particle size distribution observed in SAXS results. Furthermore, in the presence of these $Ta_{1/2}Ti_{1/2}B_2$ nanoparticles, the morphology of MgB_2 in LiMgB-10 wt.% $Ta_{1/2}Ti_{1/2}B_2$ is determined to be platelet-like (**Figures 8c, d**). This morphological change, from the bar-like MgB_2 structure observed in pure LiMgB in our previous study [50] to the platelet-like morphology of MgB_2, suggests the influence of a different nucleation center, i.e., $Ta_{1/2}Ti_{1/2}B_2$, which facilitates the formation of MgB_2 for the LiMgB-10 wt.% $Ta_{1/2}Ti_{1/2}B_2$ system. This is consistent with our previous observation of TiB_2 [50], where platelet-like MgB_2 morphology was observed to form at TiB_2 nucleation sites, rather than at Mg nucleation site in the pure LiMgB system [50]. Due to the high beam sensitivity of the LiMgB materials and the complex setup of the instrument, the interface between the nucleation center ($Ta_{1/2}Ti_{1/2}B_2$) and the newly formed phase (MgB_2) could not be investigated by HR-TEM. Instead, we employed the Edge-to-Edge matching model [51] to determine the orientation relationships between the nucleation sites and the newly formed phases (see **Section 3.3.1**).

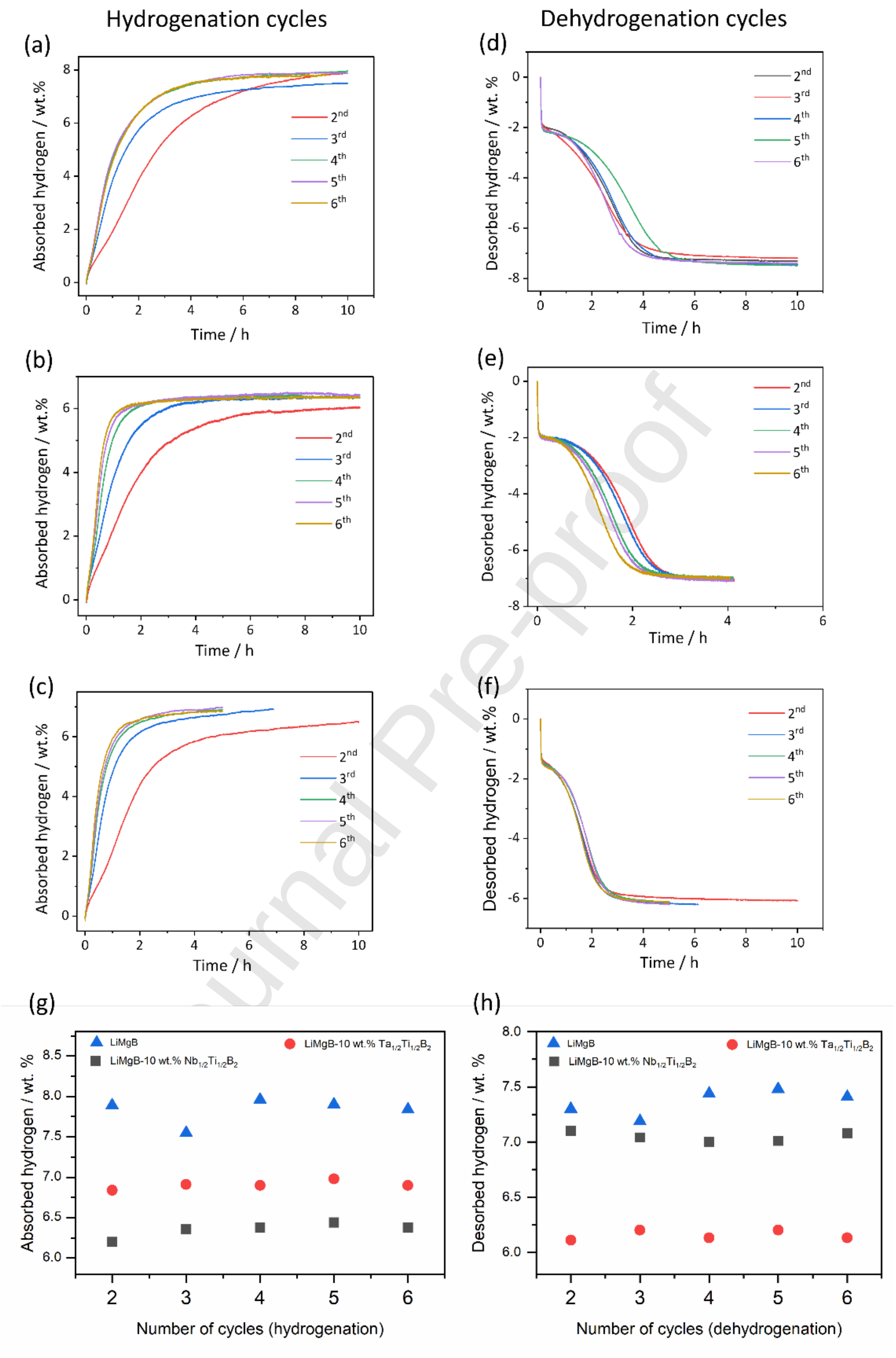

Figure 7. Hydrogenation and dehydrogenation cycles: (**a, d**) Hydrogenation-dehydrogenation cycles of the pure LiMgB, (**b, e**) Hydrogenation-dehydrogenation cycles of the LiMgB-10wt.%$Nb_{1/2}Ti_{1/2}B_2$, and (**c, f**) Hydrogenation-dehydrogenation cycles of the LiMgB-10wt.%$Ta_{1/2}Ti_{1/2}B_2$. Cycling capacity versus number of cycles for the pure and doped samples: (**g**) hydrogenation and (**h**) dehydrogenation.

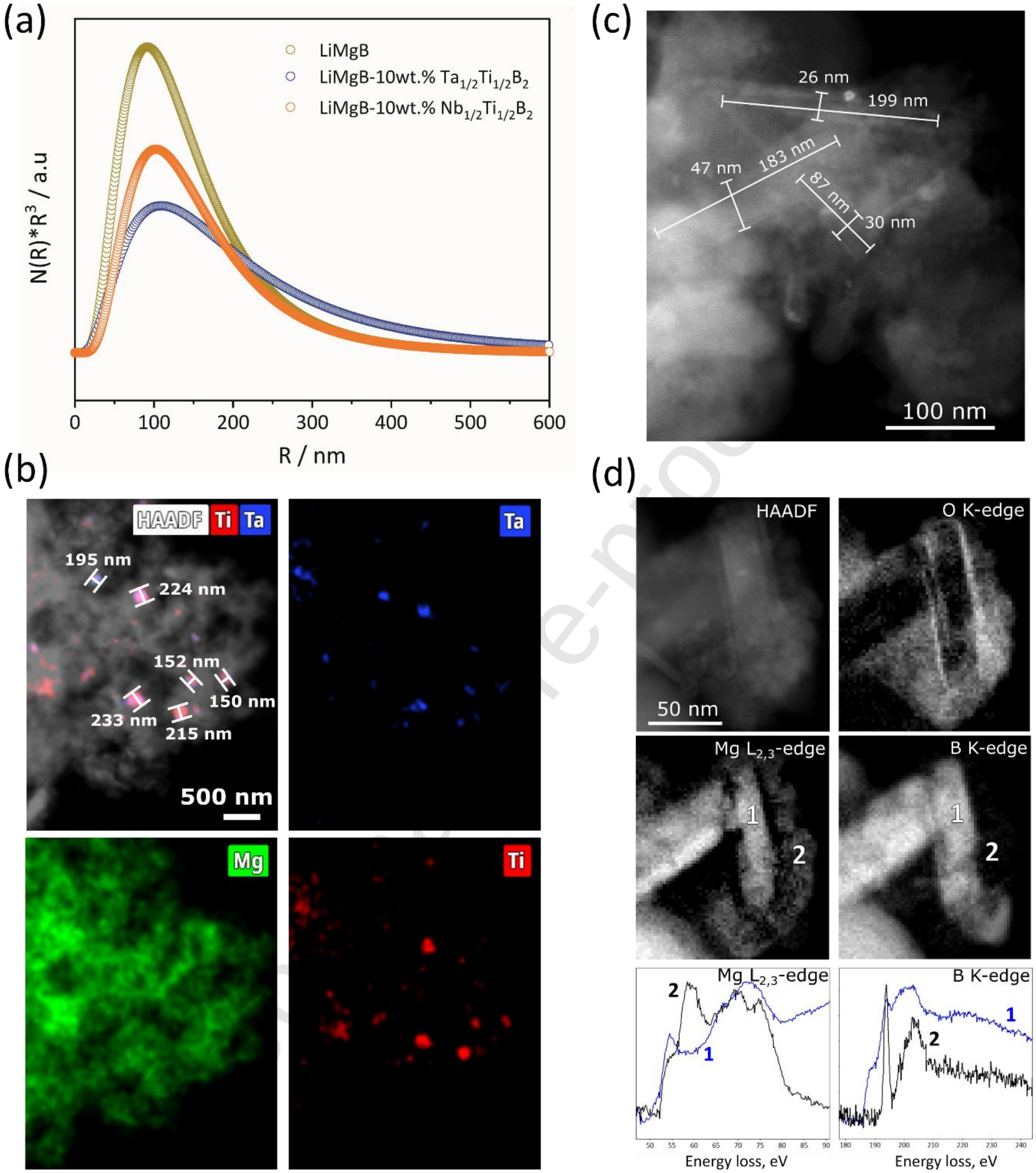

Figure 8. (**a**) Volume-weighted size distribution function of particles in pure and doped LiMgB samples after dehydrogenation obtained from SAXS data. STEM-EDS analysis for the LiMgB-10 wt. % $Ta_{1/2}Ti_{1/2}B_2$ after dehydrogenation: (**b**) STEM-HAADF and EDX elemental map of Mg (green), Ta (blue) and Ti (red). (**c**) STEM image of MgB_2 particle and (**d**) EELS analysis showing elemental distribution of B K-edge and Mg L-edge in areas (1) and (2).

It should be noted that the relatively large initial particle size of the synthesized additives up to 90 µm could negatively impact catalytic performance. This is because it could reduce the available interfacial area for contact between the catalyst and the host matrix (LiMgB), decreasing the density of accessible active sites for nanoscale solid-state reactions, thereby constraining catalytic efficiency. However, nanoscale catalyst particles are particularly susceptible to sintering, whereby they agglomerate and grow in size when exposed to high temperatures or reactive environments. This can reduce their surface area and catalytic efficiency. In this study, the $Nb_{1/2}Ti_{1/2}B_2$ and $Ta_{1/2}Ti_{1/2}B_2$ additives were incorporated into the host material and then subjected to extensive ball milling to substantially reduce the particle size and their dispersions. TEM investigation after thermal cycling confirmed that the catalyst particles had been refined to a nanoscale range of approximately 150-230 nm. This increases the interfacial area and makes more catalytic sites available, thereby improving catalytic activity. Future work will focus on optimizing the refining of particle sizes to maximize interfacial interactions and catalytic performance.

3.3. Role of the $Nb_{1/2}Ti_{1/2}B_2$ and $Ta_{1/2}Ti_{1/2}B_2$ additives

3.3.1. Lattice mismatch between newly formed phases (MgB_2, MgH_2) and parent phases ($Nb_{1/2}Ti_{1/2}B_2$ and/or $Ta_{1/2}Ti_{1/2}B_2$)

Compared to the pristine material LiMgB, the addition of $Nb_{1/2}Ti_{1/2}B_2$ or $Ta_{1/2}Ti_{1/2}B_2$ particles significantly improves the hydrogenation/dehydrogenation kinetics of the LiMgB. For all additives, whether externally added or in situ formed, the key requirement for acting as effective heterogeneous nucleation sites is to achieve maximum atomic matching between the newly formed phase and the parent phase, thereby minimizing the interfacial energy across the interface for nucleation. According to the matching rules [51], the crystallographic matching is determined by a small interatomic spacing misfit (f_s) less than 10 % in the matching directions between two phases. In addition, the matching directions must lie in matching planes where the interplanar spacing mismatch (f_d) of close-packed planes below 6 %. This allows an orientation relationship to be established between the newly formed phase and parent phase, as assessed by the f_s and f_d values. Close-packed planes are identified by the structure factor (F_{hkl}) and the interplanar spacing (d_{hkl}), where higher values of F_{hkl} and d_{hkl} yield the smaller area per atom (A_{hkl}) in the (hkl) plane, indicating a more tightly packed configuration [52]. These values (i.e., F_{hkl} and d_{hkl}) depend on the unit cell's lattice parameters.

In this study, we calculated the interplanar and interatomic spacing misfit between the parent phases (i.e., $Nb_{1/2}Ti_{1/2}B_2$, and $Ta_{1/2}Ti_{1/2}B_2$) and the newly formed phases (i.e., MgB_2, and MgH_2). The structures of MgB_2 (a=b=3.074 Å, c=3.534 Å), $Nb_{1/2}Ti_{1/2}B_2$ (a=b=3.060 Å, c=3.256Å), and $Ta_{1/2}Ti_{1/2}B_2$ (a=b=3.055 Å, c= 3.2544 Å) are all hexagonal close-packed (*hcp*) with slightly different lattice parameters. Consequently, their close-packed planes are $\{10\bar{1}1\}$, $\{10\bar{1}0\}$ and $\{0002\}$ for MgB_2 and $\{10\bar{1}1\}$, $\{10\bar{1}0\}$, and $\{0001\}$ for $Nb_{1/2}Ti_{1/2}B_2$ and $Ta_{1/2}Ti_{1/2}B_2$. In contrast, MgH_2 (a=b=4.5164 Å, c=3.021 Å) adopts a tetragonal structure (*s.g.* $P4_2/mnm$) with possible close-packed planes being {101}, {110}, and {200}. We evaluated the interplanar spacing mismatch (f_d) between these potential matching planes. Two matching plane pairs with less than 6% mismatch were identified between MgB_2 and the parent phases (X = $Nb_{1/2}Ti_{1/2}B_2$ or $Ta_{1/2}Ti_{1/2}B_2$) are $\{\mathbf{10\bar{1}1}\}_{\boldsymbol{X}} // \{\mathbf{10\bar{1}1}\}_{\mathbf{MgB_2}}$, and $\{\mathbf{10\bar{1}0}\}_{\boldsymbol{X}} // \{\mathbf{10\bar{1}0}\}_{\mathbf{MgB_2}}$**.** For MgH_2, a single plane pair was identified as $\{\mathbf{10\bar{1}0}\}_{\boldsymbol{X}} // \{\mathbf{101}\}_{\mathbf{MgH_2}}$. However, in the *hcp* systems, a small lattice mismatch between close-packed planes alone is insufficient to form orientation relationships between MgB_2 (or MgH_2) and $Nb_{1/2}Ti_{1/2}B_2$ (or $Ta_{1/2}Ti_{1/2}B_2$) phases. To ensure accurate alignment, the close-packed atomic directions within the matching planes must also have an interatomic spacing mismatch below 10%. MgB_2, $Nb_{1/2}Ti_{1/2}B_2$ and $Ta_{1/2}Ti_{1/2}B_2$ exhibit four common close-packed directions [53-55]: $\langle 11\bar{2}0\rangle$ (straight atomic row) and $\langle 10\bar{1}0\rangle$, $\langle 0001\rangle$, and $\langle 11\bar{2}3\rangle$ (zigzag atomic rows). For optimal atomic matching across the interface, straight atomic rows should match with straight ones, and zigzag rows with zigzag ones [51]. Accordingly, three matching direction pairs with interatomic mismatch below 10% on the identified matching planes between MgB_2 and *X* were found $\langle\mathbf{11\bar{2}0}\rangle_{\boldsymbol{X}} // \langle\mathbf{11\bar{2}0}\rangle_{\mathbf{MgB_2}}$, $\langle\mathbf{11\bar{2}3}\rangle_{\boldsymbol{X}} // \langle\mathbf{11\bar{2}3}\rangle_{\mathbf{MgB_2}}$, and $\langle\mathbf{0001}\rangle_{\boldsymbol{X}} // \langle\mathbf{0001}\rangle_{\mathbf{MgB_2}}$. While, for the body-centered-tetragonal (*bct*) structure of MgH_2, the nearly close-packed atom directions on the relevant planes are $\langle 11\bar{1}\rangle$ and $\langle 001\rangle$ on {110}; and $\langle 11\bar{1}\rangle$ and $\langle 010\rangle$ on {101}. Among these, the direction pair $\langle\mathbf{11\bar{2}3}\rangle_{\mathbf{X}} // \langle\mathbf{010}\rangle_{\mathbf{MgH_2}}$, lying within the matching planes pair $\{\mathbf{10\bar{1}0}\}_{\mathbf{X}} // \{\mathbf{101}\}_{\mathbf{MgH_2}}$, showed an interatomic spacing misfit of less than 2%. While the calculated interplanar mismatch and interatomic spacing misfit between the parent phases ($Nb_{1/2}Ti_{1/2}B_2$ and $Ta_{1/2}Ti_{1/2}B_2$) and the newly formed phases (MgB_2, and MgH_2) are provided in **ESI-Tables S3-S4**, **Figure 9** summarizes the identified atom matching directions on the matching planes between MgB_2 (or MgH_2) and the parent phases. The results indicate that the $Nb_{1/2}Ti_{1/2}B_2$ and $Ta_{1/2}Ti_{1/2}B_2$ nanoparticles can establish orientation relationships with both MgB_2 and MgH_2, suggesting their potential role as heterogeneous nucleation sites for the formation of MgB_2 (during dehydrogenation) and for MgH_2 (during hydrogenation). This capability could significantly improve the kinetics of both hydrogenation and dehydrogenation processes.

However, it is important to note that the direct addition of synthesized $Nb_{1/2}Ti_{1/2}B_2$ and $Ta_{1/2}Ti_{1/2}B_2$ particles into the LiMgB composite during milling may lead to a less uniform distribution of these additives than expected, which can in turn reduce overall performance of the doped composite, as similarly observed with the in-house synthesized $AlTi_3$ additive [56].

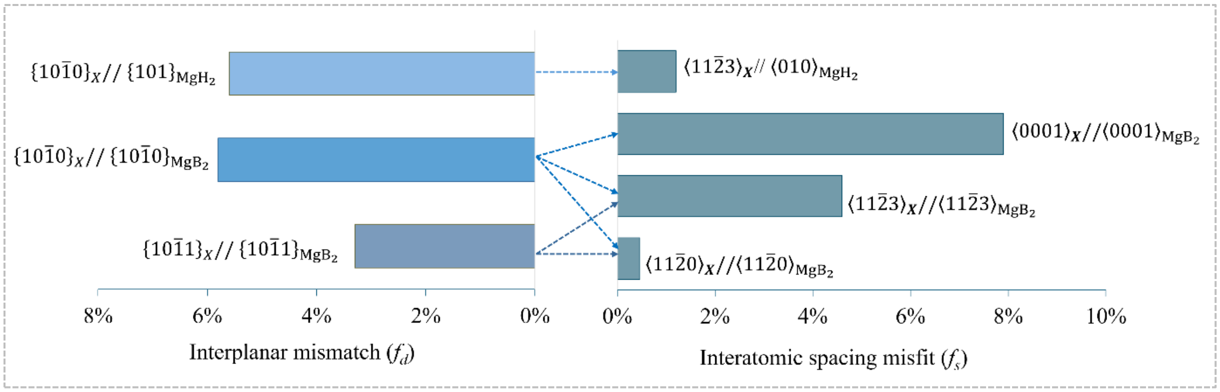

Figure 9. Interplanar and interatomic spacing mismatch between parent phase ***X*** (with X = $Nb_{1/2}Ti_{1/2}B_2$ or $Ta_{1/2}Ti_{1/2}B_2$) and newly formed phase (MgB_2, or MgH_2).

3.3.2. Rate-limiting step of hydrogenation and dehydrogenation processes

Gas-solid reaction models as described in [57] were used to evaluate the rate-limiting step in the hydrogen uptake and release process. The analysis is focused on determining how the addition of $Nb_{1/2}Ti_{1/2}B_2$ and $Ta_{1/2}Ti_{1/2}B_2$ had an impact on the rate-limiting step in hydrogenation/dehydrogenation kinetics of LiMgB composite system. The fitting procedure [21, 56] follows the methods of Sharp and Jone [58, 59], where the most appropriate reaction model is identified by linear fitting, with the highest correlation coefficient (R^2) and a straight line through the origin with a slope close to 1. In this study, different reaction kinetic equations (**ESI-Table S5**) [16] were applied to the experimental data from the 4th cycle, in order to ensure that the cycling behavior had stabilized, for the pure LiMgB and the doped LiMgB samples. The theoretical model that can describe the rate-limiting step in dehydrogenation/hydrogenation reaction kinetics the best, indicates the governing mechanistic constraint within the observed system. For the fitting procedure, only the converted fraction (α) between 0.1 and 0.8 is considered to minimize experimental uncertainties associated with the initial and final data points. **Figure 10** shows the $(t/t_{0.5})_{theoretical}$ *vs.* $(t/t_{0.5})_{experimental}$ plots of the doped samples. As a result of this fitting, the hydrogenation behavior of the LiMgB sample with the $Nb_{1/2}Ti_{1/2}B_2$ additive (**Figure 10a**) is best described by the three-dimensional contraction volume model (CV, n=3), showing the highest correlation coefficient (R^2 = 0.995), a slope close to 1, and an intercept of 0. This indicates that the hydrogenation of the LiMgB-10wt.%$Nb_{1/2}Ti_{1/2}B_2$ sample follows a phase boundary-controlled reaction, where the formation of hydrides occurs rapidly on the surface of products. The reaction rate is then governed by the progression of the reaction interface toward the center of the particles [57, 60]. Additionally, samples with different particle sizes may exhibit different hydrogenation reaction rates. In contrast, the hydrogenation behavior of the LiMgB-10wt.%$Ta_{1/2}Ti_{1/2}B_2$ sample (**Figure 10b**) aligns best with the JMA (n=1) model, which is similar to the pure LiMgB sample (**ESI-Figure S12**). This model describes a reaction mechanism involving the formation and growth of nuclei at reactions sites. Comparison of these results with the data for pristine LiMgB suggests that the addition of $Nb_{1/2}Ti_{1/2}B_2$ nanoparticles has shifted the hydrogenation mechanism in the LiMgB system from a one-dimensional, interface-controlled reaction to a three-dimensional, interface-controlled reaction. Meanwhile, the addition of $Ta_{1/2}Ti_{1/2}B_2$ does not alter the hydrogenation mechanism of LiMgB. Despite this, due to the presence of $Ta_{1/2}Ti_{1/2}B_2$ nanoparticles as nucleation sites, it promotes faster formation of MgB_2 on the $Ta_{1/2}Ti_{1/2}B_2$ particles. The activation energy for hydrogenation process was determined by fitting kinetic curves with the selected reaction model. For instance, the kinetic data of the LiMgB-10wt.%$Nb_{1/2}Ti_{1/2}B_2$ and LiMgB-10wt.%$Ta_{1/2}Ti_{1/2}B_2$ samples in the temperature range of 360-400 °C were fitted with the CV and JMA (n=1) models, respectively. The measured and fitted data of both LiMgB-10wt.%$Nb_{1/2}Ti_{1/2}B_2$ and LiMgB-10wt.%$Ta_{1/2}Ti_{1/2}B_2$ samples are in good agreement, with correlation coefficients R^2 close to 1, as seen in **ESI-Figure S13**. A kinetic rate constant (*k*) is obtained from each fitted kinetic curve (**ESI-Table S6**). The activation energies for hydrogenation and dehydrogenation for both doped samples were then obtained from the slope of the *ln(k)* vs. (*1/T*) plot. In **Figure 10c**, the activation energies of the hydrogenation process of the LiMgB-10wt.%$Nb_{1/2}Ti_{1/2}B_2$ and LiMgB-10wt.%$Ta_{1/2}Ti_{1/2}B_2$ are approximately 91 ± 3 kJ/mol H_2 and 79.5 ± 0.5 kJ/mol H_2, respectively. These activation energy values are significantly lower than that of the pure LiMgB (E_a = 184 ± 6 kJ/mol H_2) [21]. This confirms that the presence of $Nb_{1/2}Ti_{1/2}B_2$ and $Ta_{1/2}Ti_{1/2}B_2$ nanoparticles facilitates the formation of MgH_2 phase (given an atomic mismatch between MgH_2 and $Ta_{1/2}Ti_{1/2}B_2$ or $Nb_{1/2}Ti_{1/2}B_2$ in certain directions, see **Figure 9**) with correspondingly to rapid MgB_2 consumption, which prevents agglomeration and creates a more active surface area for hydrogen-material interaction. As a result, the activation energy of the hydrogenation process is reduced, thereby improving the kinetic properties compared to the pure LiMgB system.

The activation energies for the dehydrogenation process were also determined. It should be noted that the dehydrogenation process takes place in two consecutive reaction steps, where the second step is related to the reaction between Mg and $LiBH_4$ to form MgB_2, LiH and H_2 (see region II in **Figure 6 -** dehydrogenation). The dehydrogenation kinetic of these systems mainly depends on the rate of MgB_2 formation. Therefore, in this work we have determined the activation energies for the second reaction step. The fitting procedure for these two samples is equivalent to that described for pure LiMgB [21]. **Figure 10d** presents the activation energies for the dehydrogenation of the LiMgB-10wt.% $Nb_{1/2}Ti_{1/2}B_2$ and LiMgB-10wt.%$Ta_{1/2}Ti_{1/2}B_2$ samples. The activation energy of the LiMgB-10wt.%$Nb_{1/2}Ti_{1/2}B_2$ sample is estimated to be 261 ± 16 kJ/mol H_2, which is 15 kJ/mol H_2 lower than that of the LiMgB-10wt.%$Ta_{1/2}Ti_{1/2}B_2$ sample (E_a = 276 ± 7 kJ/mol H_2). Both values are lower than the activation energy of the pure sample (E_a = 293 ± 12 kJ/mol H_2) [21], and are comparable to the previously reported value for LiMgB doped with the in-house synthesized $AlTi_3$ additive (E_a = 270 ± 5 kJ/mol H_2) [56]. These results are in good agreement with the kinetic behavior reported above for the materials studied. Besides, analysis of the kinetic data indicates that the $Ta_{1/2}Ti_{1/2}B_2$-doped sample has a higher activation energy (E_a = 276 kJ/mol) than the $Nb_{1/2}Ti_{1/2}B_2$-doped sample (E_a = 261 kJ/mol). However, the former exhibits slightly faster kinetics during dehydrogenation. This can be explained to the higher pre-exponential factor, A, (*e.g.* 42.3 for $Ta_{1/2}Ti_{1/2}B_2$ versus 39.0 for $Nb_{1/2}Ti_{1/2}B_2$) - known as frequency of collisions, which offsets the higher energy barrier and accelerates the overall reaction rate. These results emphasize the importance of considering both (E_a) and (A) when evaluating reaction kinetics, since the pre-exponential factor can have a compensating or even dominant influence, depending on the system and temperature.

In addition, our first-principles study of the interfacial property of TiB_2/MgB_2 interfaces revealed that the most stable interface is found for the interface between the B-terminated MgB_2 $\{0001\}$ surface and the Ti-terminated TiB_2 $\{0001\}$ surface [33]. Thermodynamically, this suggests that TiB_2 is a favorable nucleation site for MgB_2 during dehydrogenation. Furthermore, analysis of the most stable interface (B-Ti) using net atomic charge (NAC), electron localization function (ELF), and DOS showed strong interfacial interactions at the interfacial region with the highest work of adhesion. As $Nb_{1/2}Ti_{1/2}B_2$ and $Ta_{1/2}Ti_{1/2}B_2$ are structural variants of TiB_2 with comparable crystallographic and electronic properties, it is expected that they will exhibit similar surface energies, interfacial bonding behaviors and electronic properties. Consequently, the conclusions drawn from the TiB_2/MgB_2 interface analysis are likely to be applicable to these ternary boride additives, further reinforcing their role as effective nucleation sites for MgB_2.

Recent studies have demonstrated the potential of MXene-derived catalysts to improve the performance of LiMgB composites. For instance, TiB_2 synthesized from Ti_3C_2N MXene [61] has been shown to accelerate the kinetics of hydrogen desorption in the LiMgB system. This is attributed to the partial in situ formation of TiB_2 nanoparticles, which act as nucleation agents for MgB_2 formation. Similarly, Nb-based MXenes [62, 63] have exhibited enhanced catalytic activity, likely due to complex multiphase interfacial interactions. While these studies employed different catalyst design strategies, our work utilizing $Nb_{1/2}Ti_{1/2}B_2$ and $Ta_{1/2}Ti_{1/2}B_2$ also achieve fast hydrogenation–dehydrogenation kinetics via a similar catalytic mechanism, in which $Nb_{1/2}Ti_{1/2}B_2$ and $Ta_{1/2}Ti_{1/2}B_2$ also serve as heterogeneous nucleation agents for MgB_2 formation. The comparisons highlight the wide range of catalyst design approaches used to modulate the hydrogen storage behavior of the LiMgB system, thereby emphasizing the relevance and impact of our results.

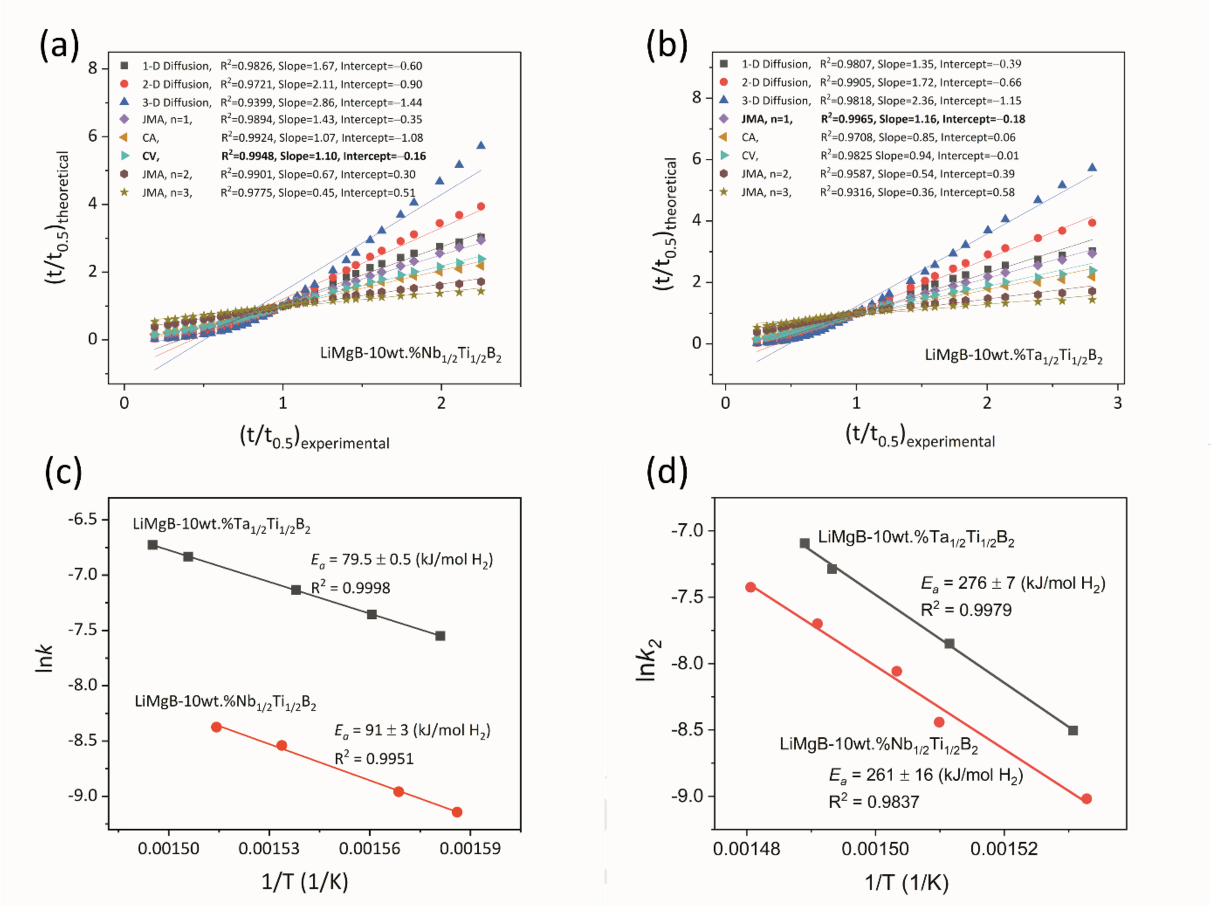

Figure 10. Kinetic modelling of (**a**) LiMgB-10wt.% $Nb_{1/2}Ti_{1/2}B_2$, and (**b**) LiMgB-10wt.% $Ta_{1/2}Ti_{1/2}B_2$ samples. (**c**) Hydrogenation and (**d**) dehydrogenation activation energies of the LiMgB-10wt.%$Nb_{1/2}Ti_{1/2}B_2$ and LiMgB-10wt.%$Ta_{1/2}Ti_{1/2}B_2$ samples, calculated from fitted kinetic data.

4. Conclusion

In this study, we used advanced computational and characterization methods to design and test additives (based on Nb-Ti-B and Ta-Ti-B) for the improvement of the kinetic properties of a model multicomponent hydrogen storage material, i.e. 2LiH-MgB_2. The results demonstrated the effectiveness of this method, paving the way for the development of new, highly effective additives for hydrogen storage applications. In particular we could demonstrate that: (i) $Nb_{1/2}Ti_{1/2}B_2$ and $Ta_{1/2}Ti_{1/2}B_2$ compositions are experimentally proven to be effective in enhancing the hydrogen absorption/desorption kinetics of the 2LiH-MgB_2 system at least twofold compared to the pure system; (ii) the presence of $Nb_{1/2}Ti_{1/2}B_2$ and $Ta_{1/2}Ti_{1/2}B_2$ nanoparticles as nucleation sites lowers the activation energy barrier for MgB_2 formation, resulting in faster kinetics in the dehydrogenation process of the 2LiH-MgB_2 composite system.

Acknowledgements

This research is funded by dtec.bw – Digitalization and Technology Research Center of Bundeswehr which we gratefully acknowledge. This work was partly carried out with the support of the Karlsruhe Nano Micro Facility (KNMFi, www.knmf.kit.edu), a Helmholtz Research Infrastructure at Karlsruhe Institute of Technology (KIT, www.kit.edu).

Author contributions

T. T. Le: writing-original draft, methodology, formal analysis, investigation, validation. **J. Cao**: Writing – original draft (part of simulation), formal analysis. **S. Korneychuk** and **A. Pundt:** Investigation. **W. Chang, M. W. Rackel** and **J. Markmann**: resources. **F. Karimi**: Methodology. **T. Klassen**: Funding acquisition. **D. Kramer**: project administration, supervision. **C. Pistidda**: conceptualization, project administration, supervision. All authors contributed to reviewing and editing this paper.

Conflicts of interest

There are no conflicts to declare.

Data Availability Statement

All data supporting this article are available in the main text or the supporting information. Raw data is available upon request.

References

[1] A. Hassanpouryouzband, E. Joonaki, K. Edlmann, R.S. Haszeldine, Offshore Geological Storage of Hydrogen: Is This Our Best Option to Achieve Net-Zero?, ACS Energy Letters 6 (2021) 2181-2186.
[2] A. Züttel, A. Borgschulte, L. Schlapbach, Hydrogen as a Future Energy Carrier, (2007).
[3] L. Schlapbach, A. Züttel, Hydrogen-storage materials for mobile applications, Nature 414 (2001) 353.
[4] D.P. Broom, C.J. Webb, G.S. Fanourgakis, G.E. Froudakis, P.N. Trikalitis, M. Hirscher, Concepts for improving hydrogen storage in nanoporous materials, International Journal of Hydrogen Energy 44 (2019) 7768-7779.
[5] 2025 DOE Technical Targets for Onboard Hydrogen Storage for Light-Duty Vehicles, https://www.energy.gov/.

[6] H. Lee, J.-w. Lee, D.Y. Kim, J. Park, Y.-T. Seo, H. Zeng, I.L. Moudrakovski, C.I. Ratcliffe, J.A. Ripmeester, Tuning clathrate hydrates for hydrogen storage, Nature 434 (2005) 743-746.
[7] J. Florusse Louw, J. Peters Cor, J. Schoonman, C. Hester Keith, A. Koh Carolyn, F. Dec Steven, N. Marsh Kenneth, E.D. Sloan, Stable Low-Pressure Hydrogen Clusters Stored in a Binary Clathrate Hydrate, Science 306 (2004) 469-471.
[8] D.P. Broom, Hydrogen Storage Materials: The Characterisation of Their Storage Properties, Springer London2011.

[9] A. Psoma, G. Sattler, Fuel cell systems for submarines: from the first idea to serial production, Journal of Power Sources 106 (2002) 381-383.

[10] G.P. Metallurgy, Off-grid stand alone: HY2 system, (2018).

[11] A. Züttel, P. Wenger, S. Rentsch, P. Sudan, P. Mauron, C. Emmenegger, LiBH4 a new hydrogen storage material, Journal of Power Sources 118 (2003) 1-7.

[12] C. Milanese, T.R. Jensen, B.C. Hauback, C. Pistidda, M. Dornheim, H. Yang, L. Lombardo, A. Zuettel, Y. Filinchuk, P. Ngene, P.E. de Jongh, C.E. Buckley, E.M. Dematteis, M. Baricco, Complex hydrides for energy storage, International Journal of Hydrogen Energy 44 (2019) 7860-7874.

[13] G. Barkhordarian, T. Klassen, M. Dornheim, R. Bormann, Unexpected kinetic effect of MgB2 in reactive hydride composites containing complex borohydrides, Journal of Alloys and Compounds 440 (2007) L18-L21.

[14] J.J. Vajo, S.L. Skeith, F. Mertens, Reversible Storage of Hydrogen in Destabilized LiBH4, The Journal of Physical Chemistry B 109 (2005) 3719-3722.

[15] U. Bösenberg, S. Doppiu, L. Mosegaard, G. Barkhordarian, N. Eigen, A. Borgschulte, T.R. Jensen, Y. Cerenius, O. Gutfleisch, T. Klassen, M. Dornheim, R. Bormann, Hydrogen sorption properties of MgH2–LiBH4 composites, Acta Materialia 55 (2007) 3951-3958.

[16] G. Gizer, J. Puszkiel, H. Cao, C. Pistidda, T.T. Le, M. Dornheim, T. Klassen, Tuning the reaction mechanism and hydrogenation/dehydrogenation properties of 6Mg(NH2)29LiH system by adding LiBH4, International Journal of Hydrogen Energy 44 (2019) 11920-11929.

[17] S. Shen, W. Liao, Z. Cao, J. Liu, H. Wang, L. Ouyang, Enhanced hydrogen storage properties of MgH2 with the co-addition of LiBH4 and YNi5 alloy, Journal of Materials Science & Technology 178 (2024) 90-99.

[18] V. Bérubé, G. Radtke, M. Dresselhaus, G. Chen, Size effects on the hydrogen storage properties of nanostructured metal hydrides: A review, International Journal of Energy Research 31 (2007) 637-663.

[19] L.E.R. Vega, D.R. Leiva, R.M. Leal Neto, W.B. Silva, R.A. Silva, T.T. Ishikawa, C.S. Kiminami, W.J. Botta, Mechanical activation of TiFe for hydrogen storage by cold rolling under inert atmosphere, International Journal of Hydrogen Energy 43 (2018) 2913-2918.

[20] R.B. Strozi, J. Ivanisenko, N. Koudriachova, J. Huot, Effect of HPT on the First Hydrogenation of LaNi5 Metal Hydride, Energies 14 (2021) 6710.

[21] T.T. Le, C. Pistidda, J. Puszkiel, M.V. Castro Riglos, F. Karimi, J. Skibsted, S.P. Gharibdoust, B. Richter, T. Emmler, C. Milanese, A. Santoru, A. Hoell, M. Krumrey, E. Gericke, E. Akiba, T.R. Jensen, T. Klassen, M. Dornheim, Design of a Nanometric AlTi Additive for MgB2-Based Reactive Hydride Composites with Superior Kinetic Properties, Journal of Physical Chemistry C 122 (2018) 7642-7655.

[22] U. Bösenberg, J.W. Kim, D. Gosslar, N. Eigen, T.R. Jensen, J.M.B. von Colbe, Y. Zhou, M. Dahms, D.H. Kim, R. Günther, Role of additives in LiBH4–MgH2 reactive hydride composites for sorption kinetics, Acta Materialia 58 (2010) 3381-3389.

[23] U. Bosenberg, U. Vainio, P.K. Pranzas, J.M. von Colbe, G. Goerigk, E. Welter, M. Dornheim, A. Schreyer, R. Bormann, On the chemical state and distribution of Zr- and V-based additives in reactive hydride composites, Nanotechnology 20 (2009) 204003.

[24] F. Karimi, M.V.C. Riglos, A. Santoru, A. Hoell, V.S. Raghuwanshi, C. Milanese, N. Bergemann, C. Pistidda, P. Nolis, M.D. Baro, G. Gizer, T.-T. Le, P.K. Pranzas, M. Dornheim, T. Klassen, A. Schreyer, J. Puszkiel, In Situ Formation of TiB2 Nanoparticles for Enhanced Dehydrogenation/Hydrogenation Reaction Kinetics of LiBH4–MgH2 as a Reversible Solid-State Hydrogen Storage Composite System, The Journal of Physical Chemistry C 122 (2018) 11671-11681.

[25] Y. Shang, O. Jin, J.A. Puszkiel, F. Karimi, P. Dansirima, C. Sittiwet, R. Utke, S. Soontaranon, T.T. Le, G. Gizer, D.V. Szabó, S. Wagner, C. Kübel, T. Klassen, M. Dornheim, A. Pundt, C. Pistidda, Effects of metal-based additives on dehydrogenation process of 2NaBH4 + MgH2 system, International Journal of Hydrogen Energy 47 (2022) 37882-37894.

[26] O. Jin, Y. Shang, X. Huang, X. Mu, D.V. Szabó, T.T. Le, S. Wagner, C. Kübel, C. Pistidda, A. Pundt, Microstructural Study of MgB2 in the LiBH4-MgH2 Composite by Using TEM, Nanomaterials 12 (2022).

[27] O. Jin, Y. Shang, X. Huang, D.V. Szabó, T.T. Le, S. Wagner, T. Klassen, C. Kübel, C. Pistidda, A. Pundt, Transformation Kinetics of LiBH4–MgH2 for Hydrogen Storage, Molecules 27 (2022).

[28] S. Chakravarty, D.J. Sharar, P.J. Shamberger, Heterogeneous nucleation of gallium with lattice-matched cubic carbide and nitride phases, Journal of Applied Physics 130 (2021).

[29] Z.P. Wu, D.T. Caracciolo, Y. Maswadeh, J. Wen, Z. Kong, S. Shan, J.A. Vargas, S. Yan, E. Hopkins, K. Park, A. Sharma, Y. Ren, V. Petkov, L. Wang, C.J. Zhong, Alloying-realloying enabled high durability for Pt-Pd-3d-transition metal nanoparticle fuel cell catalysts, Nat Commun 12 (2021) 859.

[30] R. Backofen, A. Voigt, A phase field crystal study of heterogeneous nucleation – application of the string method, The European Physical Journal Special Topics 223 (2014) 497-509.

[31] B. Jiang, Y. Yuan, W. Wang, K. He, C. Zou, W. Chen, Y. Yang, S. Wang, V. Yurkiv, J. Lu, Surface lattice engineering for fine-tuned spatial configuration of nanocrystals, Nature Communications 12 (2021) 5661.

[32] H. Zhang, X. Jin, J.-M. Lee, X. Wang, Tailoring of Active Sites from Single to Dual Atom Sites for Highly Efficient Electrocatalysis, ACS Nano 16 (2022) 17572-17592.

[33] Y. Shang, A. Santhosh, P. Jerabek, T. Klassen, C. Pistidda, First-principles study on interfacial property in MgB2-based reactive hydride composites, Scripta Materialia 240 (2024) 115837.

[34] T. Fiantok, N. Koutná, D.G. Sangiovanni, M. Mikula, Ceramic transition metal diboride superlattices with improved ductility and fracture toughness screened by ab initio calculations, Scientific Reports 13 (2023) 12835.

[35] I. Bressler, J. Kohlbrecher, A.F. Thunemann, : a tool for small-angle scattering data analysis using a library of analytical expressions, J Appl Crystallogr 48 (2015) 1587-1598.

[36] G. Kresse, J. Hafner, Ab initio molecular dynamics for liquid metals, Physical Review B 47 (1993) 558-561.

[37] G. Kresse, J. Furthmüller, Efficient iterative schemes for ab initio total-energy calculations using a plane-wave basis set, Physical Review B 54 (1996) 11169-11186.

[38] G. Kresse, J. Furthmüller, Efficiency of ab-initio total energy calculations for metals and semiconductors using a plane-wave basis set, Computational Materials Science 6 (1996) 15-50.

[39] J.P. Perdew, K. Burke, M. Ernzerhof, Generalized Gradient Approximation Made Simple, Physical Review Letters 77 (1996) 3865-3868.

[40] G. Kresse, D. Joubert, From ultrasoft pseudopotentials to the projector augmented-wave method, Physical Review B 59 (1999) 1758-1775.

[41] B. Puchala, A. Van der Ven, Thermodynamics of the Zr-O system from first-principles calculations, Physical Review B 88 (2013) 094108.

[42] J.C. Thomas, A.V.d. Ven, Finite-temperature properties of strongly anharmonic and mechanically unstable crystal phases from first principles, Physical Review B 88 (2013) 214111.

[43] https://github.com/prisms-center/CASMcode.

[44] B. Puchala, J.C. Thomas, A.R. Natarajan, J.G. Goiri, S.S. Behara, J.L. Kaufman, A. Van der Ven, CASM — A software package for first-principles based study of multicomponent crystalline solids, Computational Materials Science 217 (2023) 111897.

[45] A. Van der Ven, J.C. Thomas, B. Puchala, A.R. Natarajan, First-Principles Statistical Mechanics of Multicomponent Crystals, Annual Review of Materials Research 48 (2018) 27-55.

[46] W. Qiao, S. Yan, D. Jin, X. Xu, W. Mi, D. Wang, Vertical-orbital band center as an activity descriptor for hydrogen evolution reaction on single-atom-anchored 2D catalysts, Journal of Physics: Condensed Matter 33 (2021) 245201.

[47] Q. Li, X. Zou, X. Ai, H. Chen, L. Sun, X. Zou, Revealing Activity Trends of Metal Diborides Toward pH-Universal Hydrogen Evolution Electrocatalysts with Pt-Like Activity, Advanced Energy Materials 9 (2019) 1803369.

[48] Y. Yao, Z. Zhang, L. Jiao, Development Strategies in Transition Metal Borides for Electrochemical Water Splitting, ENERGY & ENVIRONMENTAL MATERIALS 5 (2022) 470-485.

[49] L. Lutterotti, S. Matthies, H.R. Wenk, A.S. Schultz, J.W. Richardson, Combined texture and structure analysis of deformed limestone from time-of-flight neutron diffraction spectra, Journal of Applied Physics 81 (1997) 594-600.

[50] O. Jin, Y. Shang, X. Huang, X. Mu, D.V. Szabó, T.T. Le, S. Wagner, C. Kübel, C. Pistidda, A. Pundt, Microstructural Study of MgB2 in the LiBH4-MgH2 Composite by Using TEM, Nanomaterials 12 (2022) 1893.

[51] M.X. Zhang, P.M. Kelly, Edge-to-edge matching model for predicting orientation relationships and habit planes—the improvements, Scripta Materialia 52 (2005) 963-968.

[52] P.M. Kelly, H.P. Ren, D. Qiu, M.X. Zhang, Identifying close-packed planes in complex crystal structures, Acta Materialia 58 (2010) 3091-3095.

[53] J. Yang, J.L. Wang, Y.M. Wu, L.M. Wang, H.J. Zhang, Extended application of edge-to-edge matching model to HCP/HCP (α-Mg/MgZn2) system in magnesium alloys, Materials Science and Engineering: A 460-461 (2007) 296-300.

[54] M.X. Zhang, P.M. Kelly, Edge-to-edge matching and its applications: Part I. Application to the simple HCP/BCC system, Acta Materialia 53 (2005) 1073-1084.

[55] M.X. Zhang, P.M. Kelly, M.A. Easton, J.A. Taylor, Crystallographic study of grain refinement in aluminum alloys using the edge-to-edge matching model, Acta Materialia 53 (2005) 1427-1438.

[56] T.T. Le, C. Pistidda, J. Puszkiel, M.V.C. Riglos, D.M. Dreistadt, T. Klassen, M. Dornheim, Enhanced hydrogen storage properties of Li-RHC system with in-house synthesized AlTi3 nanoparticles, Energies 14 (2021) 7853.

[57] A. Khawam, D.R. Flanagan, Solid-State Kinetic Models: Basics and Mathematical Fundamentals, The Journal of Physical Chemistry B 110 (2006) 17315-17328.

[58] L.F. Jones, D. Dollimore, T. Nicklin, Comparison of experimental kinetic decomposition data with master data using a linear plot method, Thermochimica Acta 13 (1975) 240-245.

[59] J.H. Sharp, G.W. Brindley, B.N.N. Achar, Numerical Data for Some Commonly Used Solid State Reaction Equations, Journal of the American Ceramic Society 49 (1966) 379-382.

[60] Z. Zhou, L. Han, G.M. Bollas, Kinetics of NiO reduction by H2 and Ni oxidation at conditions relevant to chemical-looping combustion and reforming, International Journal of Hydrogen Energy 39 (2014) 8535-8556.

[61] H. Luo, Y. Yang, L. Lu, G. Li, X. Wang, X. Huang, X. Tao, C. Huang, Z. Lan, W. Zhou, J. Guo, H. Liu, Highly-dispersed nano-TiB2 derived from the two-dimensional Ti3CN MXene for tailoring the kinetics and reversibility of the Li-Mg-B-H hydrogen storage material, Applied Surface Science 610 (2023) 155581.

[62] L.-W. Lu, H. Luo, G.-X. Li, Y. Li, X.-H. Wang, C.-K. Huang, Z.-Q. Lan, W.-Z. Zhou, J. Guo, M. Ismail, H.-Z. Liu, Layered niobium carbide enabling excellent kinetics and cycling stability of Li-Mg-B-H hydrogen storage material, Rare Metals 43 (2024) 1153-1166.

[63] H. Liu, L. Lu, H. Luo, J. Deng, G. Li, H. Ning, Y. Fan, C. Huang, Z. Lan, W. Zhou, J. Guo, X. Wang, Hybrid of bulk NbC and layered Nb4C3 MXene for tailoring the hydrogen storage kinetics and reversibility of Li–Mg–B–H composite: An experimental and theoretical study, Journal of Materials Science & Technology 194 (2024) 225-235.

Declaration of interests

☒The authors declare that they have no known competing financial interests or personal relationships that could have appeared to influence the work reported in this paper.

☐The authors declare the following financial interests/personal relationships which may be considered as potential competing interests:

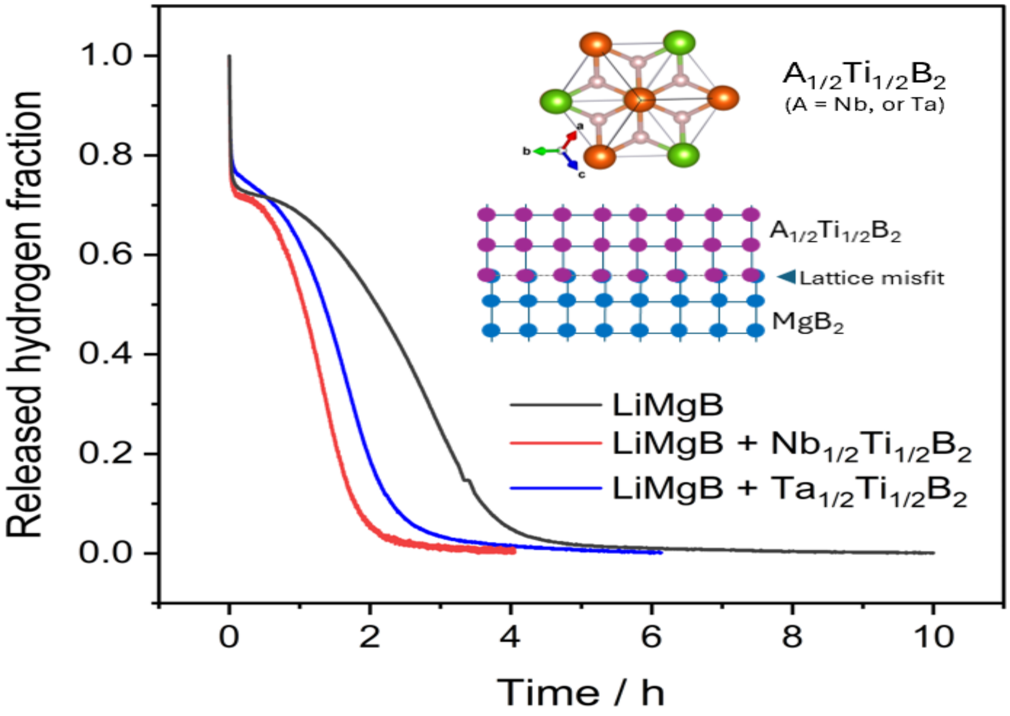
Released hydrogen fraction
1.0
0.8
0.6
0.4
0.2
0.0
0
2
4
6
8
10
Time / h
$A_{1/2}Ti_{1/2}B_2$
(A = Nb, or Ta)
a
b
c
$A_{1/2}Ti_{1/2}B_2$
Lattice misfit
MgB_2
LiMgB
LiMgB + $Nb_{1/2}Ti_{1/2}B_2$
LiMgB + $Ta_{1/2}Ti_{1/2}B_2$

Highlights

- Computational - experimental approach used to design Nb-Ti-B and Ta-Ti-B additives for hydrogen storage.
- $Nb_{1/2}Ti_{1/2}B_2$ and $Ta_{1/2}Ti_{1/2}B_2$ catalysts double hydrogen absorption/desorption kinetics of the 2LiH-MgB_2 system.
- $Nb_{1/2}Ti_{1/2}B_2$ and $Ta_{1/2}Ti_{1/2}B_2$ nanoparticles serve as nucleation sites, reducing the activation energy for MgB_2 formation.
- Validating a rational design strategy for next-generation hydrogen storage additives.